Tunable goniopolarity of graphenelike boron layers in metal diborides

Siyun Qi, Jian Liu, Yangyang Li, and Mingwen Zhao[*]

School of Physics, Shandong University, Jinan 250100, China

The orientation-dependent conduction polarity, e.g., p-type conduction along one direction and n-type conduction along another direction, namely "goniopolarity," observed in highly anisotropic materials brought us an alternative concept for novel electronic devices. But goniopolarity has hardly been utilized due to the rarity of goniopolar materials. Here, we associate goniopolarity with the saddle points in electronic band structure and the hyperbolic Fermi surface of materials and highlight the potential of layered metal diboride (MB$_2$) materials in achieving this interesting phenomenon using first-principles calculations. We demonstrate that the electron-doped MgB$_2$, CaB$_2$, and SrB$_2$ can exhibit remarkable orientation-dependent conduction polarity with opposite Seebeck coefficients which are detectable in verifying goniopolarity. We attribute the goniopolarity with the $p_{x,y}$ orbitals of the boron layers of these materials which constitute anisotropic electronic states along in-plane and out of plane directions. Moreover, their anisotropic Seebeck coefficients can be efficiently enhanced by applying tensile strain. This work offers a promising strategy for design of goniopolar materials and regulation of goniopolarity.

I. INTRODUCTION

The conversion of the electric energy and thermal energy arising from the orientation movement of carriers has been a key subject in both scientific research and practical applications [1,2], where carrier modulation plays a crucial role. Conventional semiconducting materials are either p type or n type, depending on the polarity of the majority carriers. The integration of p-type and n-type semiconductors in heterojunctions [3,4] constitutes the basis of modern electronic technologies, such as diodes [5,6], photodetectors [7], and solar cells [8]. Representative examples are the silicon-based semiconductors where the polarity of the majority carriers exhibit isotropic features and can be regulated by dopants [9,10].

Interestingly, opposite signs of Hall coefficients in different directions have been found in recent experiments [11], suggesting the orientation-dependent conduction polarity in these materials. In other words, these materials can be featured by n-type semiconductors along one direction but p-type semiconductors along another direction, which is named as "goniopolarity." The coexistence of intrinsic n and p types of semiconducting features in these goniopolar materials alters the conventional concept in developing multifunction electronic devices. Moreover, the anisotropic Seebeck coefficients arising from the orientation-dependent carrier polarity bring us new possibilities for transverse thermoelectrics [12]. For example, the heat flow transverse to electrical current in goniopolar materials in the absence of external magnetic fields holds great potential in cryogenic temperatures.

Layered materials with distinguishable anisotropy along the in-plane and out of plane directions are naturally considered as promising candidates of goniopolar materials. Despite the abundant layered materials, only a few of them have been demonstrated to show strong anisotropic thermoelectric properties, such as SnSe [6], NaSn$_2$As$_2$ [11], Ti$_2$SiC$_2$ [13], Mg$_2$Sn [14], BaF$_2$As$_2$ [15], CsBi$_4$Te$_6$ [16], and hexagonal group-II metals (Mg, Zn, and Cd) [17] suggesting the strict requirements of achieving goniopolarity. The rarity of goniopolar materials and the unclear relation between goniopolarity and lattice characteristics (e.g., atomic orbitals) highly limit the investigation and application of goniopolarity.

The discovery of superconducting MgB$_2$ with a high critical temperature (T_c) around 39 K almost reaching the McMillan limit has attracted great attention [18–20]. MgB$_2$ has graphitelike B layers intercalated by hexagonal stacked metal atoms, as shown in Fig. 1(a). The interband anisotropy enhances the coupling constant from the isotropic dirty-limit value to clean-limit value [21]. The zone-center phonon frequencies, transport properties, and broadband hyperbolic light dispersion of MgB$_2$ and other metal diborides (MB$_2$) have been intensively explored [22,23]. The Seebeck effects in MgB$_2$ have been intensively investigated both theoretically and experimentally [24–28]. The sign change of Seebeck coefficients in electron-doped MgB$_2$ has been predicted [27], suggesting the potential goniopolarity in MB$_2$ materials. However, the correlation between the orientation-dependent conduction polarity and the electronic band structures of MB$_2$ materials remains unclear. There have been few reports of the Seebeck coefficients of the MB$_2$ materials beyond MgB$_2$.

In view of the correlation between goniopolarity and anisotropy of materials [29], in this contribution, we conduct extensive investigation on the goniopolar properties of 14 MB$_2$ materials, from which we highlight the role of the saddle point of electronic band structures in the goniopolarity of MB$_2$ materials and propose two promising candidates
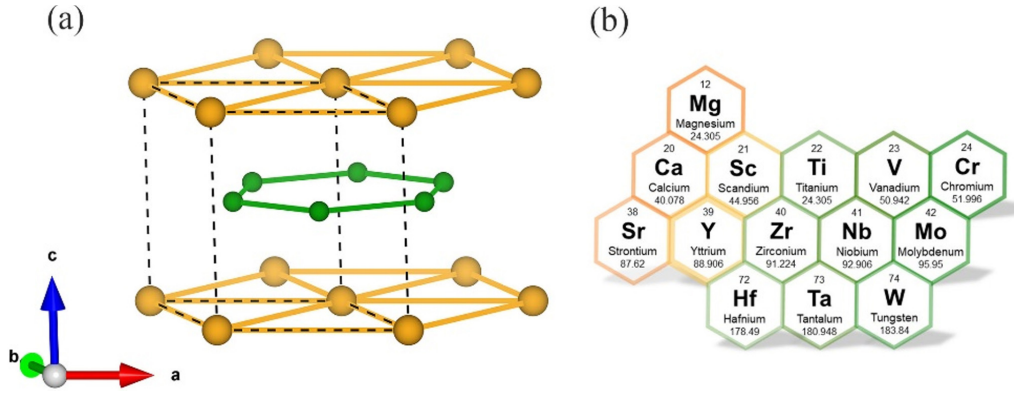
---

*zmw@sdu.edu.cn

FIG. 1. (a) Crystal structure of metal diborides (MB$_2$). (b) Fourteen MB$_2$ materials selected from the Materials Project database. Orange and green balls indicate metal and B atoms, respectively.

(CaB$_2$ and SrB$_2$) in addition to MgB$_2$ with remarkable orientation-dependent conduction polarity and Seebeck effect. Our calculations reveal the existence of saddle points in the electronic band structures and the hyperbolic Fermi surfaces of MB$_2$ ($M =$ Mg, Ca, Sr), which is associated with the $p_{x,y}$ orbitals of the graphenelike boron layers. The goniopolarity of these MB$_2$ materials was further verified from the Seebeck coefficients with opposite polarity along the in-plane and out of plane directions. Moreover, the goniopolarity can be efficiently enhanced by applying tensile strain. This work offers a universal strategy for design and regulation of goniopolarity, as well as promising candidate goniopolar materials.

II. METHOD AND COMPUTATIONAL DETAILS

Our calculations are performed by the QUANTUM ES-PRESSO package using the framework of functional theory (DFT) [30]. The electron-ion interaction is described by projector-augmented wave (PAW) potential and the generalized gradient approximation (GGA) in the form of Perdew-Burke-Ernzerhof (PBE) is adopted for the exchange-correlation functional [31]. The electrons wave functions are expanded using the plane-wave basis with the energy cutoff and the charge density cutoff of 50 and 500 Ry, respectively [32]. The self-consistent electron density is evaluated by a k-point mesh of $12 \times 12 \times 12$. The lattice constants are fully optimized with the energy convergence set to 10^{-8} eV and force convergence set to 5×10^{-4} eV/Å [33]. The electron doping effect is simulated by adding electrons to the supercell, while a homogeneous background charge with opposite sign is assumed to keep the electrical neutrality of the system. The mechanical properties are calculated from the strain in response to the out of plane lattice distortion.

The wave vector dependent electron relaxation time $\tau(\mathbf{k})$ is calculated from the electron-phonon coupling matrix elements via the Wannier interface [34,35]. More than twice as many bands as orbitals are considered to construct the real-space Hamiltonian in the Wannier basis [36,37]. The electron-phonon interaction and the phonon dispersion scattering matrix elements are calculated first on a $6 \times 6 \times 6$ k and q mesh [38–40]. A dense $20 \times 20 \times 20$ mesh for k and q is adopted in the calculations of carrier relaxation time due to

the electron-phonon interaction by using the EPW package [41]; also see the Supplemental Material [42].

III. RESULTS AND DISCUSSION

The metal diborides investigated in this work have layered configurations with honeycomb B and hexagonal M layers stacking alternatively along the z direction, as shown in Fig. 1(a). We consider fourteen MB$_2$ materials, as shown in Fig. 1(b), selected from the Materials Project database. The unit cell contains one M and two B atoms with a $P6/mmm$ space group. M atoms reside on the vertices of the unit cell, while B atoms occupy the sites right above the center of M regular triangles constituting a graphenelike layer. The optimized lattice constants of these MB$_2$ materials are presented in Table S1 in the Supplemental Material [42], which are consistent with the experimental data and other theoretical results [18,22]. The lattice constants decrease (increase) as M varies from the left side (top) to the right side (bottom) of the period table, which can be correlated to the trend of covalent radii of the M atoms. Charge density plots show that the bonding in the boron layer is typically covalent and a large amount of valence charges of M atoms distribute homogeneously over the crystal [43,44]. It is worth noting that although $4d$ and $5d$ transition metal (TM) atoms have similar covalent radii, MB$_2$ materials possess smaller lattice constants for $5d$ TM atoms than those for $4d$ TM atoms, suggesting stronger interaction between the M and B layers. In the following discussion, we take MgB$_2$ without d electrons as an example to explore the electronic properties and the Fermi surfaces of MB$_2$ materials.

We start from the relationship between the electronic structure and goniopolarity of MgB$_2$. The electronic band structure along highly symmetric directions of MgB$_2$ is presented in Fig. 2(a). The bands near the Fermi level can be featured by the σ bands arising from the $p_{x,y}$ orbitals of the B atoms and the π bands donated by the p_z orbitals of the B atoms, as labeled in Fig. 2(a). Notably, the σ bands form a "saddle" point in the region ~ 0.4 eV above the Fermi level at the Γ point (the dotted box). The saddle point joints two segments of a band line with opposite signs of electron effective masses (m^*). The band curves downward along the Γ-K (in-plane) direction with a negative m^*, but upward along the Γ-A (out of plane) direction with a positive m^*. Therefore, the anisotropic
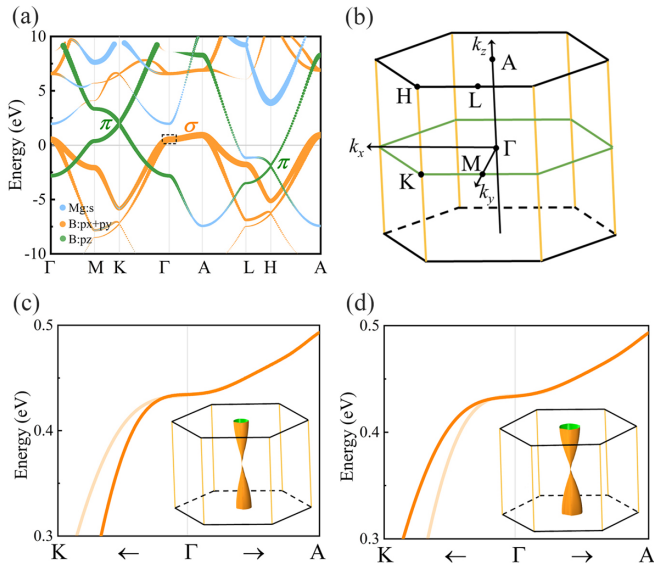
FIG. 2. (a) Electronic band structure of MgB_2, the band structure projected by $p_{x,y}$ (σ bonds, orange color) and p_z (π bonds, green color) orbit of B atom. The Fermi level is set to zero. The box with dotted lines indicates the position of the saddle points. (b) First Brillouin zone of MgB_2. (c), (d) Orbital-resolved band structure and isoenergetic surfaces of the two σ bands at the saddle point, highlighting the goniopolar mechanism.

FIG. 3. The band structures of (a) MgB_2, (b) CaB_2, and (c) SrB_2 and the Seebeck coefficients along the in-plane (S_{xx} and S_{yy}) and out of plane (S_{zz}) direction at 300 K. The shaded areas highlight the saddle points in the band structures corresponding to goniopolar regions with the opposite in-plane (S_{xx} and S_{yy}) and out of plane (S_{zz}) Seebeck coefficients.

electronic structure near the saddle point can be described by a simple expression according to the effective mass approximation (EMA) where m^* has opposite signs along the in-plane and out of plane directions. In sharp contrast to the model for conventional semiconductors, this model gives a hyperbolic Fermi surface which reflects the highly anisotropic electronic properties (see Supplemental Material [42]).

The band structures of the other 13 MB_2 materials are plotted in Fig. S2 [42]. Despite the complicated band lines of these materials, the saddle points at the Γ point that arise from the in-plane and out of plane coupling of B_σ bands are preserved, but have different positions relative to the Fermi level, due to the different amount of valence electrons of the M atoms. Similar to the case of MgB_2, CaB_2 and SrB_2 have the saddle points near the Fermi level, as shown in Fig. 3, and thus are expected to contribute to the orientation-dependent conduction polarity properties upon electron doping. Additionally, the band structure in the region near the saddle point should be as "clean" as possible to avoid the contributions of other trivial bands which may suppress the goniopolarity. Therefore, in the following section, we focus on the goniopolarity of MgB_2, CaB_2, and SrB_2. Notably, the orbital-resolved electronic band structures near the saddle point of these three MB_2 materials show the same features contributed by the p_x and p_y orbitals of the B atoms (see Supplemental Material [42]).

Thermoelectric materials are the functional materials that can directly convert temperature difference to electric voltage and vice versa via a thermocouple. The thermoelectric performance is usually characterized by Seebeck effects, which reflect the thermopower of charge carriers from the hot side to the cold side. The electric potential is built up across a temperature gradient, and the Seebeck coefficient measures
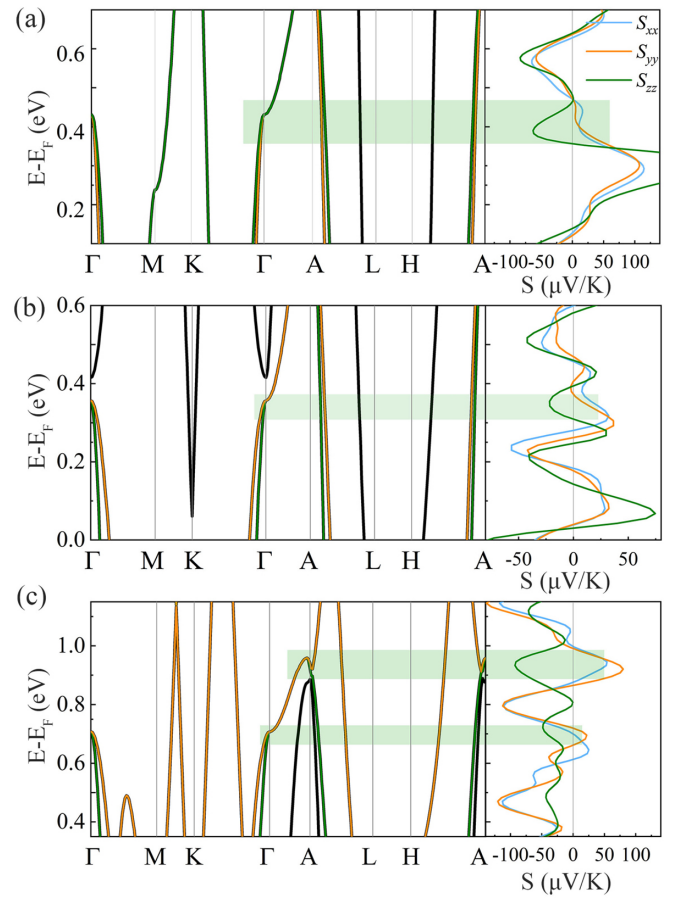
the magnitude of the induced thermoelectric voltage. The sign of the Seebeck coefficient is determined by the type of majority carriers, i.e., negative for electrons and positive for holes. Therefore, the orientation-dependent conduction polarity properties can also be described by the Seebeck coefficient along different directions.

To demonstrate the goniopolarity of these materials, we evaluated the Seebeck coefficients. The variation of Seebeck coefficients as the Fermi level moves upward (e.g., by electron doping) at room temperature is plotted in the right-hand panel of Fig. 3. S_{xx}, S_{yy}, and S_{zz} represent the Seebeck coefficients along the x, y, and z directions, respectively. It can be seen that S_{xx} and S_{yy} show similar variation trends, indicating the weak in-plane anisotropy of these materials. However, the variation of S_{zz} differs significantly from S_{xx} and S_{yy}, exhibiting a sign opposite to both S_{xx} and S_{yy} in specific energy windows, as indicated by the shaded areas. These energy windows are in good consistence with the positions of the saddle points. MgB_2 has the largest difference of Seebeck coefficient between in-plane (48 $\mu V/K$) and out of plane (–63 $\mu V/K$), which is much larger than those of $NaSn_2As_2$ (–2, 20 $\mu V/K$) [45], $BaCuAs$ (24, –39 $\mu V/K$) [29], and

TABLE I. The effective masses of electrons at the saddle points and the maximal Seebeck coefficients in the goniopolar regions at 300 K. The Seebeck coefficients are in μV/K; m_0 represent the mass of a free electron. The two saddle points of SrB$_2$ are indicated by L (low energy) and H (high energy), respectively.

Material		m^*_{xx}/m_0	m^*_{yy}/m_0	m^*_{zz}/m_0	S_{xx}	S_{yy}	S_{zz}
	0%	−0.2239	−0.4645	3.4627	38	48	−63
MgB$_2$	1%	−0.2248	−0.4656	3.5673	72	60	−67
	2%	−0.2259	−0.4667	3.7266	96	96	−60
CaB$_2$		−0.2566	−1.0003	2.0288	29	31	−22
SrB$_2$	L	−0.2367	−1.1623	2.0568	10	22	−46
	H	−0.3746	−0.3746	3.3207	53	53	−89

Al$_{13}$Co$_4$ (19, −17 μV/K) [46]. The signs of the Seebeck coefficients are also consistent with the curvatures of the bands along the in-plane direction (Γ-K and Γ-M) and out of plane direction (Γ-A), which lead to negative m^*_x and m^*_y, and positive m^*_z. Similar results are also found in CaB$_2$ and SrB$_2$. It is interesting to see that SrB$_2$ has two saddle points at the energies of 0.71 and 0.92 eV, resulting in two goniopolar regions, respectively. The largest difference between in-plane and out of plane Seebeck coefficients is142 μV/K for the high energy saddle point. For the other MB$_2$ materials, the anisotropic

features of the Seebeck coefficients are un-noticeable due to the contributions of the trivial bands without saddle points which suppress the goniopolarity.

It is noteworthy that the Seebeck coefficients of MgB$_2$ have been calculated within a rigid band strategy [27], similar to the method used in this work. The scenario of $S_{xx} = S_{xx} > 0$ and $S_{zz} < 0$ was also predicted in a specific electron doping range. However, the results of Ref. [27] differ significantly from those of the present work in the following aspects. Firstly, $|S_{xx}| > |S_{zz}|$ was predicted in that work, but our calculations give the opposite order. This may be related to the assumption of constant electron relaxation time $\tau(\mathbf{k})$ adopted in Ref. [27]. In the present work, however, $\tau(\mathbf{k})$ is calculated from the electron-phonon coupling matrix elements [34,35] which are obviously $\mathbf{k}$ dependent. Secondly, the in-plane Seebeck tensor of MgB$_2$ was proposed to be isotropic ($S_{xx} = S_{yy}$), but our calculations reveal the difference between S_{xx} and S_y. We attribute the weak in-plane anisotropy of the Seebeck tensor in MgB$_2$ to the different band profile along the Γ-K and Γ-M directions, as shown in Fig. 2(a), which leads to different effective masses of electrons (m^*_{xx} and m^*_{yy}), as listed in Table I.

We certainly need to emphasize that the MB$_2$ materials have to be doped by electrons to achieve anisotropic Seebeck effects in experiments because the saddle points are in the conduction band regions. The electronic band structure
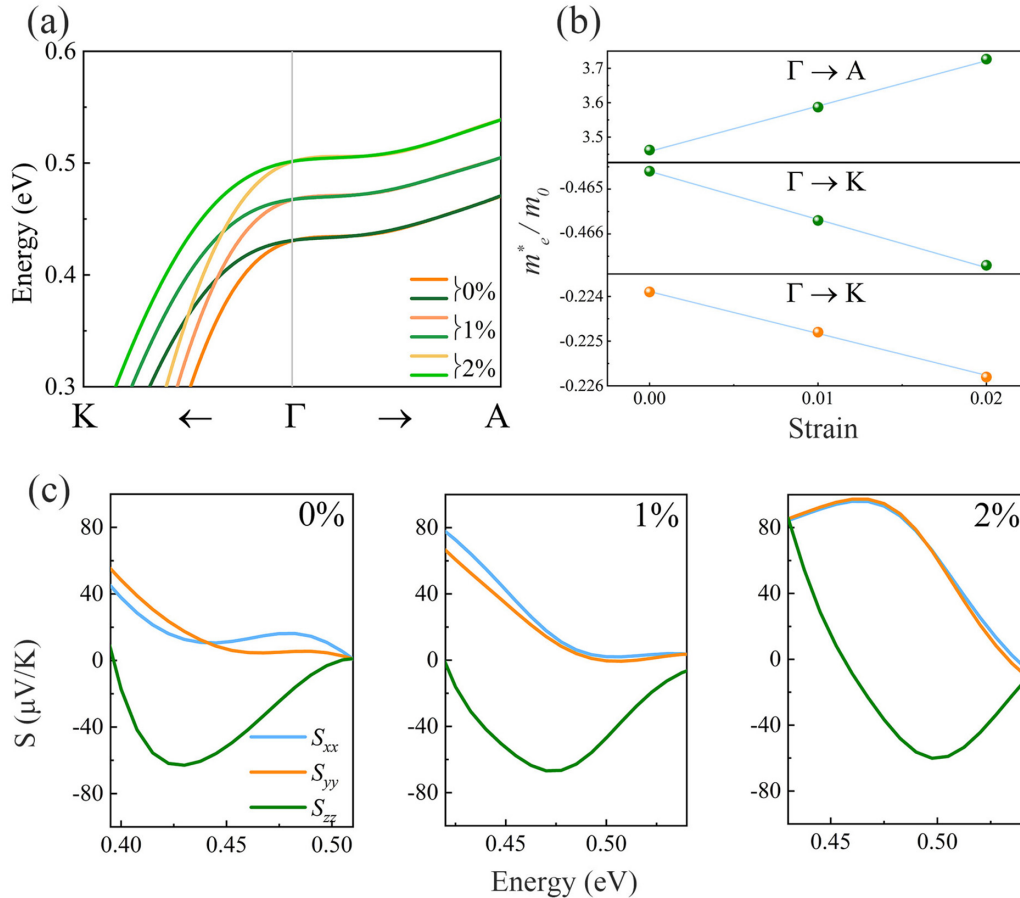

FIG. 4. The electronic structures of MgB$_2$ under uniaxial tensile strain along the z direction. (a) The enlarged band structures near the saddle points. (b) The effective mass of the bands at the Γ point along the Γ-K line and the Γ-A line. (c) The in-plane (S_{xx} and S_{yy}) and out of plane (S_{zz}) Seebeck coefficients at 300 K.

calculations of the electron-doped MB$_2$ materials show that the electron doping concentrations of 0.30, 0.34, and 1.25 electrons per unit cell for MgB$_2$, CaB$_2$, and SrB$_2$ are required to push the Fermi level to the saddle points, as shown in Fig. S3 [42]. The electronic band structures near the saddle points are preserved in these electron-doped MB$_2$ materials except for the position of the Fermi level. This can be achieved by substitutional doping of MB$_2$ with C atoms in the form of M(B$_{1-x}$C$_x$)$_2$. The dynamics stability of the electron-doped MgB$_2$ and CaB$_2$ is also verified from the phonon spectra which are free from imaginary frequency (see Supplemental Material [42]). It has been confirmed experimentally that the sign of the Seebeck coefficient changes from positive to negative in the electron-doped Mg(B$_{1-x}$C$_x$)$_2$ materials [25–28], which was attributed to the electron filling in the π bands [27]. These experimental advances suggest the plausibility of achieving anisotropic goniopolarity of MB$_2$ via electron doping. The CaB$_2$ phase considered in this work has been predicted to be a superconductor with a T_c higher than MgB$_2$ [21,47]. However, the realization of goniopolarity in CaB$_2$ material remains a challenging task due to the difficulty in synthesis of stable CaB$_2$ samples at ambient and high pressure [48]. For SrB$_2$, the plausibility of such a high electron-doping level in experiments remains an open question. Anyway, our work offers a general strategy for design of goniopolar materials, as well as potential candidate goniopolar materials beyond MgB$_2$.

Furthermore, we consider the variation of the Seebeck coefficients in response to the strain along the z direction. For the layered materials, the structural anisotropy can be regulated by applying strain along the out of plane direction, which is expected to tune the relevant properties [49–51]. Therefore, we calculate the electronic band structures and Seebeck coefficients of MgB$_2$ under tensile strains of 1% and 2% as examples to demonstrate this interesting feature. The variation of the band structure, effective mass, and the Seebeck coefficients are exhibited in Fig. 4. The saddle point is preserved under the strain, but is pushed upward with the increase of strain, as shown in Fig. 4(a). With the increase of the tensile strain, the effective mass of the band along the z direction increases slightly, whereas effective masses along the in-plane direction (Γ-K) exhibit the opposite trend, as shown in Fig. 4(b). This implies that the anisotropy in

electronic structure is enhanced under tensile strain. From the variations of the Seebeck coefficients, as shown in Fig. 4(c), one can see that the minimal value of S_{zz} ($\sim$60 μV/K) is insensitive to the tensile strain, but the changes of S_{xx} and S_{yy} are more remarkable. The maximal values of S_{xx} and S_{yy} increase to 96 μV/K under the tensile strain of 2% (Table I). The enhanced anisotropy of Seebeck coefficients under tensile strains offers a promising strategy to modulate goniopolarity, which is quite crucial for transverse thermoelectrics. Additionally, the ability of MgB$_2$ for carrier concentration optimization and phonon-scattering strengthening has been demonstrated in experiments. For example, the thermoelectric performance of In$_{0.1}$Sb$_{1.9}$Te$_3$ [52] and GeTe-based alloys [53] can be enhanced as MgB$_2$ is introduced.

IV. CONCLUSION

In summary, we demonstrate the goniopolar properties of MgB$_2$, CaB$_2$, and SrB$_2$ from first-principles calculations. We correlated the goniopolarity to the $p_{x,y}$ orbitals of graphene-like boron layers which form highly anisotropic electronic states along the Γ-K and Γ-A directions along with a saddle point at the Γ point and the hyperboloid-shaped Fermi surface. For these three metal diborides, the bands exhibit p-type (hole) characteristics with negative effective masses along the Γ-K (in-plane) direction and n-type (electron) features with positive effective masses along the Γ-A (out of plane) direction. The goniopolar properties are verified by the anisotropic Seebeck coefficients, which are positive along the in-plane directions and negative along the out of plane direction. The largest difference between the in-plane (48 μV/K) and out of plane (–63 μV/K) Seebeck coefficients is 111 μV/K in MgB$_2$. Moreover, the anisotropy of the Seebeck coefficients can be enhanced by applying tensile strain. The specific intrinsic goniopolar property leads to the discovery of unique electronic properties and provides a promising strategy for designing novel electronics and thermoelectric applications in the future.

[1] J. Lou, H. Ma, J. Wang, R. Yang, B. Dong, Y. Yu, J. Wang, F. Zhang, Y. Fan, M. Feng, Z. Li, C. Nan, and S. Qu, Adv. Electron. Mater. **6**, 1900795 (2019).

[2] T. P. Rossi, P. Erhart, and M. Kuisma, ACS Nano **14**, 9963 (2020).

[3] Y. Tang, B. Cui, C. Zhou, and M. Grayson, J. Electron. Mater. **44**, 2095 (2015).

[4] W. Shockley and H. J. Queisser, J. Appl. Phys. **32**, 510 (1961).

[5] J. U. Lee, P. P. Gipp, and C. M. Heller, Appl. Phys. Lett. **85**, 145 (2004).

[6] Z. Wang, C. Fan, Z. Shen, C. Hua, Q. Hu, F. Sheng, Y. Lu, H. Fang, Z. Qiu, J. Lu, Z. Liu, W. Liu, Y. Huang, Z. A. Xu, D. W. Shen, and Y. Zheng, Nat. Commun. **9**, 47 (2018).

[7] D. Guo, Y. Su, H. Shi, P. Li, N. Zhao, J. Ye, S. Wang, A. Liu, Z. Chen, C. Li, and W. Tang, ACS Nano **12**, 12827 (2018).

[8] B. M. Kayes, H. A. Atwater, and N. S. Lewis, J. Appl. Phys. **97**, 114302 (2005).

[9] J. G. Fossum and D. S. Lee, Solid State Electron. **25**, 741 (1982).

[10] G. Cantele, E. Degoli, E. Luppi, R. Magri, D. Ninno, G. Iadonisi, and S. Ossicini, Phys. Rev. B **72**, 113303 (2005).

[11] B. He, Y. Wang, M. Q. Arguilla, N. D. Cultrara, M. R. Scudder, J. E. Goldberger, W. Windl, and J. P. Heremans, Nat. Mater. **18**, 568 (2019).

[12] C. Zhou, S. Birner, Y. Tang, K. Heinselman, and M. Grayson, Phys. Rev. Lett. **110**, 227701 (2013).

[13] L. Chaput, G. Hug, P. Pécheur, and H. Scherrer, Phys. Rev. B **71**, 121104(R) (2005).

[14] X. Li, S. Li, S. Feng, and H. Zhong, Intermetallics **81**, 26 (2017).

[15] M. Meinero, F. Caglieris, I. Pallecchi, G. Lamura, S. Ishida, H. Eisaki, A. Continenza, and M. Putti, J. Phys.: Condens. Matter **31**, 214003 (2019).

[16] D. Chung, T. P. Hogan, M. Rocci, P. Brazis, J. R. Ireland, C. R. Kannewurf, M. Bastea, C. Uher, and M. G. Kanatzidis, J. Am. Chem. Soc. **126**, 6414 (2004).

[17] V. A. Rowe and P. A. Schroeder, J. Phys. Chem. Solids **31**, 1 (1970).

[18] A. Y. Liu, I. I. Mazin, and J. Kortus, Phys. Rev. Lett. **87**, 087005 (2001).

[19] C. Buzea and T. Yamashita, Supercond. Sci. Technol. **14**, R115 (2001).

[20] M. Kambara, N. H. Babu, E. S. Sadki, J. R. Cooper, H. Minami, D. A. Cardwell, A. M. Campbell, and I. H. Inoue, Supercond. Sci. Technol. **14**, L5 (2001).

[21] P. W. Anderson, J. Phys. Chem. Solids **11**, 26 (1959).

[22] H. Gao, X. Zhang, W. Li, and M. Zhao, Opt. Express **27**, 36911 (2019).

[23] G. Satta, G. Profeta, F. Bernardini, A. Continenza, and S. Massidda, Phys. Rev. B **64**, 104507 (2001).

[24] I. Pallecchi, M. Monni, P. Manfrinetti, and M. Putti, J. Phys.: Condens. Matter **31**, 164001 (2019).

[25] K. Rogacki, K. Oganisian, C. Sulkowski, N. Zhigadlo, S. Katrych, and J. Karpinski, J. Phys. Chem. Solids **69**, 3202 (2008).

[26] M. Matusiak, K. Rogacki, N. D. Zhigadlo, and J. Karpinski, Euro Phys. Lett. **90**, 27009 (2010).

[27] M. Putti, E. Galleani d'Agliano, D. Marrè, F. Napoli, M. Tassisto, P. Manfrinetti, A. Palenzona, C. Rizzuto, and S. Massidda, Eur. Phys. J. B **25**, 439 (2002).

[28] J. Karpinski, N. D. Zhigadlo, S. Katrych, R. Puzniak, K. Rogacki, and R. Gonnelli, Phys. C (Amsterdam) **456**, 3 (2007).

[29] Y. Wang, K. G. Koster, A. M. Ochs, M. R. Scudder, J. P. Heremans, W. Windl, and J. E. Goldberger, J. Am. Chem. Soc. **142**, 2812 (2020).

[30] P. Giannozzi, S. Baroni, N. Bonini, M. Calandra, R. Car, C. Cavazzoni, D. Ceresoli, G. L. Chiarotti, M. Cococcioni, I. Dabo, A. Dal Corso, S. de Gironcoli, S. Fabris, G. Fratesi, R. Gebauer, U. Gerstmann, C. Gougoussis, A. Kokalj, M. Lazzeri, L. Martin-Samos *et al.*, J. Phys.: Condens. Matter **21**, 395502 (2009).

[31] J. P. Perdew, K. Burke, and M. Ernzerhof, Phys. Rev. Lett. **78**, 1396 (1997).

[32] M. Methfessel and A. T. Paxton, Phys. Rev. B **40**, 3616 (1989).

[33] H. J. Monkhorst and J. D. Pack, Phys. Rev. B **13**, 5188 (1976).

[34] A. A. Mostofi, J. R. Yates, Y. Lee, I. Souza, D. Vanderbilt, and N. Marzari, Comput. Phys. Commun. **178**, 685 (2008).

[35] F. Giustino, M. L. Cohen, and S. G. Louie, Phys. Rev. B **76**, 165108 (2007).

[36] J. Noffsinger, F. Giustino, B. D. Malone, C. Park, S. G. Louie, and M. L. Cohen, Comput. Phys. Commun. **181**, 2140 (2010).

[37] S. Poncé, E. R. Margine, C. Verdi, and F. Giustino, Comput. Phys. Commun. **209**, 116 (2016).

[38] Y. Wang, J. Lv, Y. Ma, T. Cui, and G. Zou, Phys. Rev. B **80**, 092505 (2009).

[39] S. Lu, H. Liu, I. I. Naumov, S. Meng, Y. Li, J. S. Tse, B. Yang, and R. J. Hemley, Phys. Rev. B **93**, 104509 (2016).

[40] C. Liu, X. Song, Q. Li, Y. Ma, and C. Chen, Phys. Rev. Lett. **124**, 147001 (2020).

[41] B. Liao, J. Zhou, B. Qiu, M. S. Dresselhaus, and G. Chen, Phys. Rev. B **91**, 235419 (2015).

[42] See Supplemental Material at http://link.aps.org/supplemental/10.1103/PhysRevB.106.165204 for the computational details of Seebeck coefficients, the lattice parameters of MB_2, the effective mass model of goniopolarity, the electronic band structures of MB_2, the orbital-resolved band structures of intrinsic and electron-doped MB_2, and the phonon spectra of the intrinsic and electron-doped MgB_2 and CaB_2.

[43] K. P. Bohnen, R. Heid, and B. Renker, Phys. Rev. Lett. **86**, 5771 (2001).

[44] J. M. An and W. E. Pickett, Phys. Rev. Lett. **86**, 4366 (2001).

[45] Y. Wang and P. Narang, Phys. Rev. B **102**, 125122 (2020).

[46] J. Dolinšek, M. Komelj, P. Jeglič, S. Vrtnik, D. Stanić, P. Popčević, J. Ivkov, A. Smontara, Z. Jagličić, P. Gille, and Y. Grin, Phys. Rev. B **79**, 184201 (2009).

[47] H. J. Choi, S. G. Louie, and M. L. Cohen, Phys. Rev. B **80**, 064503 (2009).

[48] S. Shah and A. N. Kolmogorov, Phys. Rev. B **88**, 014107 (2013).

[49] J. Liu, Y. Zhao, C. Lian, Z. Dai, J. Sun, and S. Meng, J. Phys. Mater. **2**, 024001 (2019).

[50] H. Y. Lv, W. J. Lu, D. F. Shao, and Y. P. Sun, Phys. Rev. B **90**, 085433 (2014).

[51] K. Yamamoto, K. Masuda, K.-I. Uchida, and Y. Miura, Phys. Rev. B **101**, 094430 (2020).

[52] H. Qin, S. Sun, Y. Liu, L. Yin, Y. Zhang, Y. Sun, L. Xie, D. Qin, M. Guo, F. Guo, W. Qu, Z. Liu, Q. Zhang, W. Cai, H. Wu, and J. Sui, Nano Energy **90**, 106530 (2021).

[53] L. Wang, J. Li, Y. Xie, L. Hu, F. Liu, W. Ao, J. Luo, and C. Zhang, Mater. Today Phys. **16**, 100308 (2021).